

Resonant terahertz detection using graphene plasmons

Denis A. Bandurin,^{1, a)} Dmitry Svintsov,² Igor Gayduchenko,^{3, 2} Shuigang G. Xu,^{1, 4} Alessandro Principi,¹ Maxim Moskotin,^{3, 2} Ivan Tretyakov,³ Denis Yagodkin,^{2, 3} Sergey Zhukov,² Takashi Taniguchi,⁵ Kenji Watanabe,⁵ Irina V. Grigorieva,¹ Marco Polini,^{6, 1} Gregory N. Goltsman,³ Andre K. Geim,^{1, 4} and Georgy Fedorov^{2, 3, b)}

¹⁾*School of Physics, University of Manchester, Oxford Road, Manchester M13 9PL, United Kingdom*

²⁾*Moscow Institute of Physics and Technology (State University), Dolgoprudny 141700, Russia*

³⁾*Physics Department, Moscow State University of Education (MSPU), Moscow, 119435, Russian Federation*

⁴⁾*National Graphene Institute, University of Manchester, Manchester M13 9PL, United Kingdom*

⁵⁾*National Institute for Materials Science, 11 Namiki, Tsukuba, 3050044 Japan*

⁶⁾*Istituto Italiano di Tecnologia, Graphene Labs, Via Morego 30, 16163 Genova, Italy*

Plasmons, collective oscillations of electron systems, can efficiently couple light and electric current, and thus can be used to create sub-wavelength photodetectors, radiation mixers, and on-chip spectrometers. Despite considerable effort, it has proven challenging to implement plasmonic devices operating at terahertz frequencies. The material capable to meet this challenge is graphene as it supports long-lived electrically-tunable plasmons. Here we demonstrate plasmon-assisted resonant detection of terahertz radiation by antenna-coupled graphene transistors that act as both plasmonic Fabry-Perot cavities and rectifying elements. By varying the plasmon velocity using gate voltage, we tune our detectors between multiple resonant modes and exploit this functionality to measure plasmon wavelength and lifetime in bilayer graphene as well as to probe collective modes in its moiré minibands. Our devices offer a convenient tool for further plasmonic research that is often exceedingly difficult under non-ambient conditions (e.g. cryogenic temperatures) and promise a viable route for various photonic applications.

Selective detection and spectroscopy of THz fields is a challenging task in modern optoelectronics offering a wide range of applications: from security and medical inspection to radio astronomy and wireless communications^{1,2}. Among the variety of available detection principles², one elegant proposal has always stood out and remained intriguing for more than two decades. The idea is to compress incident radiation into highly-confined two-dimensional plasmons propagating in the field effect transistor (FET) channel and to rectify the induced ac potential using the same device³. The FET channel, in this case, acts as a tunable plasmonic cavity with a set of resonant frequencies defined by its length and the density of charge carriers. The implementation of such resonant devices has promised on-chip selective sensing, spectroscopy, mixing, and modulation of THz fields below the classical diffraction limit³. However, despite decades-long experimental efforts, the excitation of long-lived plasma oscillations in conventional FETs has proven challenging⁴⁻⁹ and little evidence of resonant THz detection has been found so far¹⁰⁻¹⁴.

Graphene has recently demonstrated great promise for mid- and far-infrared plasmonics¹⁵⁻²² and attracted a great deal of attention as a platform for plasmonic radiation detectors^{19,23}. With lowering the operation frequency down to the THz domain, the resonant excitation

of plasmons becomes exceedingly difficult and can only be achieved if the momentum relaxation rate is below the plasmon frequency, which, in turn, requires ultra-high electron mobility. For this reason, in all graphene-based far-field THz detectors reported so far, the plasma waves – if any – were overdamped, and the devices exhibited only a broadband (non-resonant) photoresponse^{5-9,24,25}. As a result, numerous applications relying on resonant plasmon excitation (see e.g. Refs. 3, 26–29) remain experimentally yet unrealized.

In this work, we demonstrate this long-sought resonant regime using FETs based on high-quality van der Waals heterostructures. In particular, we employ graphene encapsulated between hexagonal boron nitride (hBN) crystals which have been shown to provide the cleanest environment for long-lived graphene plasmons^{20,22}. Antenna-mediated coupling of such FETs to free-space radiation results in the emergence of dc photovoltage that peaks when the channel hosts an odd number of plasmon quarter-wavelengths. Exploiting the gate-tunability of plasmon velocity, we switch our detectors between more than ten resonant modes, and use this functionality to measure plasmon wavelength and lifetime. Thanks to the far-field radiation coupling, our compact devices offer a convenient tool for studies of plasmons in two-dimensional electron systems under non-ambient conditions (e.g. cryogenic environment and high magnetic fields) where other techniques may be arduous. As an example, we apply our approach to probe plasmons in graphene/hBN superlattices and unveil collective modes

^{a)}Electronic mail: bandurin.d@gmail.com

^{b)}Electronic mail: fedorov.ge@mipt.ru

These authors contributed equally: D.A. Bandurin and D. Svintsov

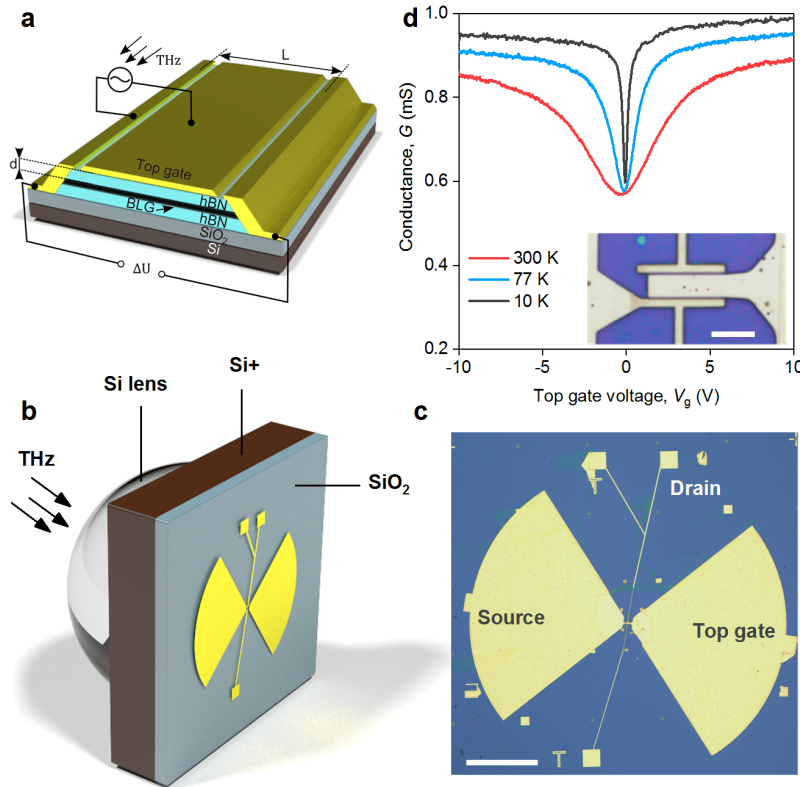


FIG. 1. **Graphene-based THz detectors.** **a**, Schematics of the encapsulated BLG FET used in this work. **b**, 3D rendering of our resonant photodetector. THz radiation is focused to a broadband bow-tie antenna by a hemispherical silicon lens yielding modulation of the gate-to-source voltage, as indicated in (a). **c**, Optical photograph of one of our photodetectors. Scale bar is $200 \mu\text{m}$. **d**, Conductance of one of our BLG FETs as a function of the gate voltage V_g , measured at a few selected temperatures. Inset: Zoomed-in photograph of (c) showing a two-terminal FET with gate and source terminals connected to the antenna. Scale bar is $10 \mu\text{m}$.

of charge carriers in moiré minibands.

RESULTS

Graphene-based THz detectors

There are three crucial steps to consider in the design of resonant photodetectors. First, the incoming radiation needs to be efficiently compressed into plasmons propagating in the FET channel. Second, the channel should act as a high-quality plasmonic cavity, where constructive interference of propagating plasma waves leads to the enhancement of the field strength. Third, the high-frequency plasmon field needs to be rectified into a dc photovoltage. To meet these hard-to-satisfy^{5–8} requirements, we fabricated proof-of-concept detectors using high-mobility bilayer graphene (BLG) FETs. To this end, we first applied a standard dry transfer technique to encapsulate BLG between two relatively thin ($d \approx 80 \text{ nm}$) slabs of hBN³⁰. The heterostructure had side contacts (Fig. 1a) which were extended to the millimeter scale and one of them served as a sleeve of the broadband antenna, Fig. 1c and Supplementary Fig. 3a-b (see Methods). Another antenna sleeve was connected to the top gate covering the FET channel (inset of Fig. 1d).

In this coupling geometry, the incident radiation induces high-frequency modulation of the gate-to-channel voltage thereby launching plasma waves from the source terminal³. The detector was assembled on a THz-transparent Si wafer attached to a Si lens focusing the incident radiation onto the antenna (Fig. 1b).

We studied four BLG FETs, from 3 to $6 \mu\text{m}$ in length L and from 6 to $10 \mu\text{m}$ in width W , all exhibiting typical field-effect behaviour as seen from measurements of the conductance G (Fig. 1d and Supplementary Fig. 3e). In particular, G is minimal at the charge neutrality point and rises with increasing V_g . The mobility of our devices at the characteristic carrier density $n = 10^{12} \text{ cm}^{-2}$ exceeded $10 \text{ m}^2/\text{Vs}$ and remained above $2 \text{ m}^2/\text{Vs}$ at temperatures $T = 10 \text{ K}$ and 300 K , respectively, as determined from the characterization of a multiterminal Hall bar produced under identical protocol reported in Methods (Supplementary Note 1 and Supplementary Fig. 1).

Broadband operation

We intentionally start the photoresponse measurements at the low end of the sub-THz domain, where the plasma oscillations are overdamped (see below). This allows us

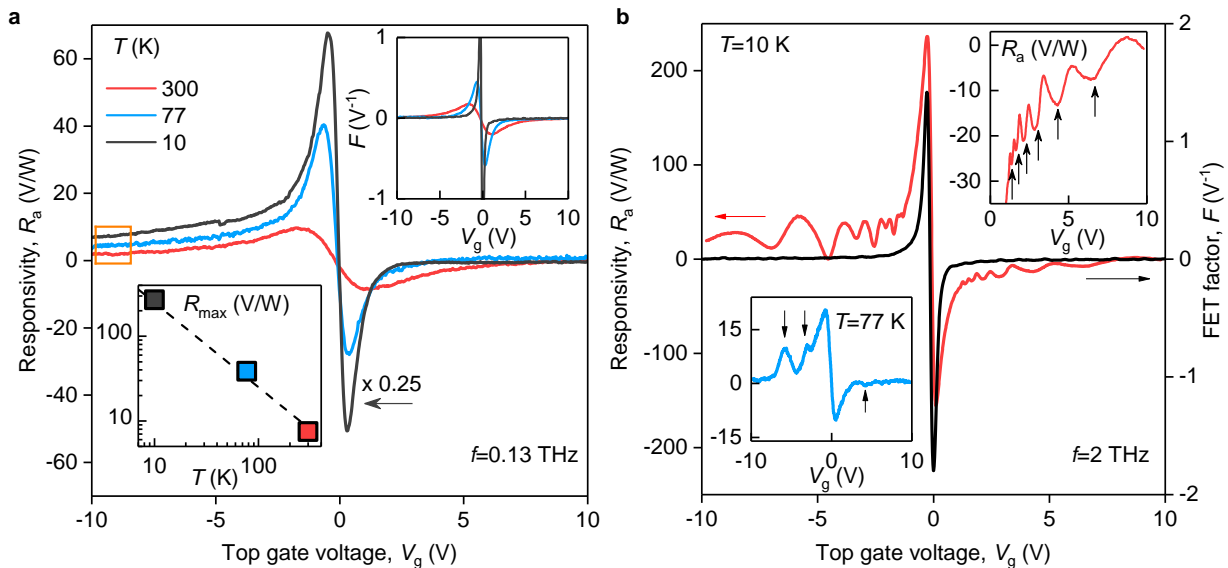


FIG. 2. **Plasmon-assisted resonant THz photodetection.** **a**, Responsivity measured at $f = 130$ GHz and three representative temperatures. Orange rectangle highlights an offset stemming from the rectification of incident radiation at the p-n junction between the p-doped graphene channel and the n-doped area near the contact. Upper inset: FET-factor F as a function of V_g at the same T . Lower inset: Maximum R_a as a function of T . **b**, Gate dependence of responsivity recorded under 2 THz radiation. The upper inset shows a zoomed-in region of the photovoltage for electron doping. Resonances are indicated by black arrows. Lower inset: resonant responsivity at liquid-nitrogen temperature.

to compare the performance of our detectors with previous reports^{5–8,23}. Figure 2a shows an example of the responsivity $R_a = \Delta U/P$, where ΔU is the emerging source-to-drain photovoltage and P is the incident radiation power, as a function of the top gate voltage V_g under irradiation with frequency $f = 0.13$ THz in one of our BLG detectors (see Methods). In good agreement with the previous studies, the $R_a(V_g)$ dependence follows the evolution of the FET-factor $F = -\frac{1}{\sigma} \frac{d\sigma}{dV_g}$, shown in the inset of Fig. 2a. In particular, R_a increases in magnitude upon approaching the charge neutrality point (NP) where it flips sign because of the change in charge carrier type.

We have studied the operation of our detectors at different temperatures and found that R_a grows with decreasing T (bottom inset of Fig. 2a) and reaches its maximum $R_a \approx 240$ V/W at $T = 10$ K due to a steeper $F(V_g)$ at this T (top inset of Fig. 2a). At large positive V_g , R_a approaches zero at all T , whereas at negative V_g , a positive offset is observed (orange rectangle in Fig. 2a). This behaviour is common for this type of devices and is related to additional rectification by p-n junctions at the boundaries between the p-doped graphene channel and the n-doped contact regions^{24,31,32}.

The overall broadband responsivity of our BLG detectors is further improved in transistors with stronger nonlinearity, which can be conveniently parametrized by the FET-factor introduced above. To this end, we took advantage of the gate-tunable band structure of BLG and fabricated a dual-gated photodetector. Simultaneous action of the two gates results in a band gap opening and

a steep $F(V_g)$ dependence that, in turn, causes a drastic enhancement of R_a (Supplementary Note 2). The latter exceeded 3 kV/W for a weak displacement field D of 0.1 V/nm (Supplementary Fig. 2b). This translates to the noise equivalent power (NEP) of about 0.2 pW/Hz^{1/2}, estimated using the Johnson-Nyquist noise spectral density obtained for the same D . The observed performance of our detectors makes them competitive not only with other graphene-based THz detectors operating in the broadband regime²³, but also with some commercial superconducting and semiconductor bolometers operating at the same f and T (Supplementary Table 1).

Resonant photoresponse

The response of our photodetectors changes drastically as the frequency of incident radiation is increased. Fig. 2b shows the gate voltage dependence of R_a recorded in response to 2 THz radiation. In stark contrast to Fig. 2a, R_a exhibits prominent oscillations, despite the fact that F as a function of V_g is featureless (black curve in Fig. 2b). The oscillations are clearly visible for both electron and hole doping and display better contrast on the hole side, likely because of the aforementioned p-n junction rectification. Resonances are well discerned at 10 K, although they persist up to liquid-nitrogen T , especially for $V_g < 0$. A further example of resonant operation of another BLG device is shown in Supplementary Note 3.

We have also studied the performance of our detectors at intermediate frequencies and found that the resonant operation of our devices onsets in the middle of the sub-THz domain (Supplementary Note 4). In partic-

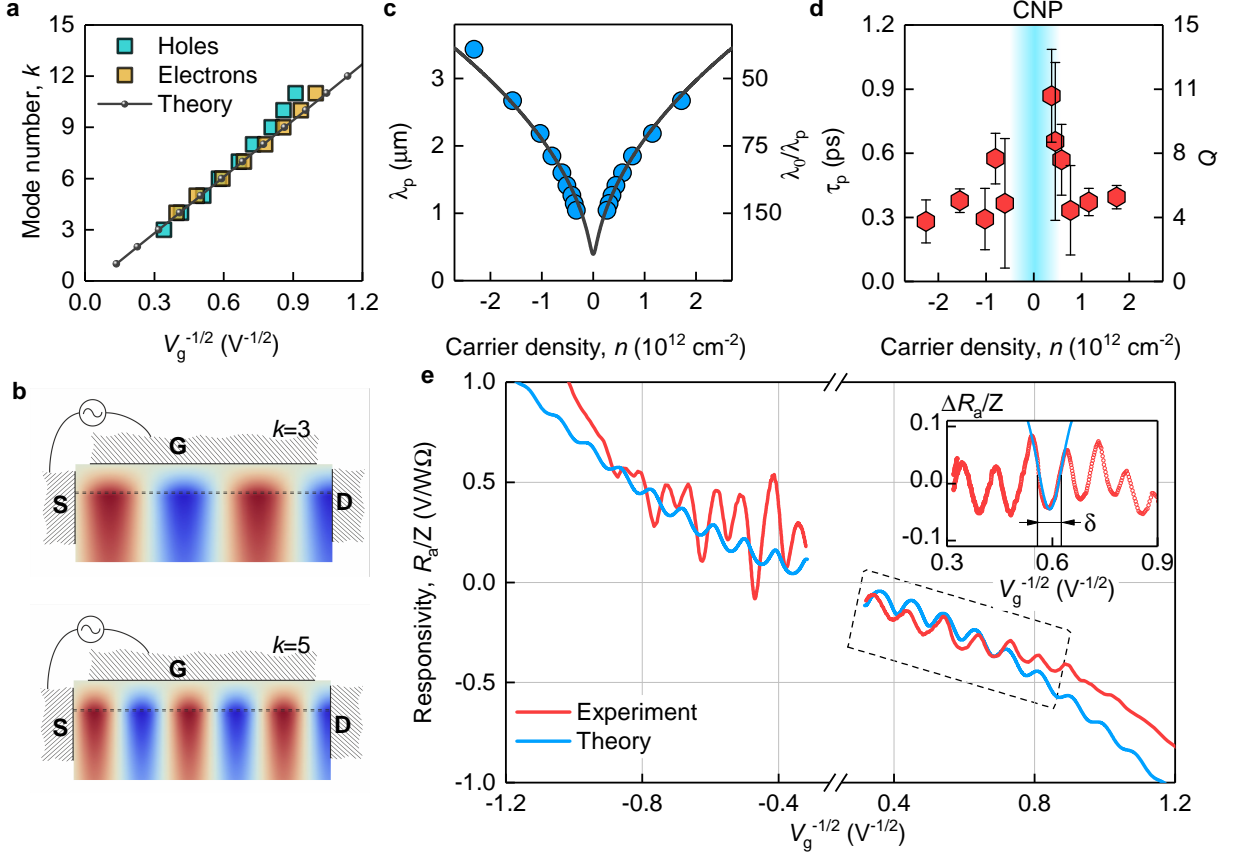


FIG. 3. **Plasmon resonances in encapsulated-graphene FET.** **a**, Mode number k as a function of $V_g^{-1/2}$ (symbols). Solid line: Theoretical dependence for $L = 6 \mu\text{m}$, $m = 0.036m_e$ and $f = 2 \text{ THz}$. The first mode supported by our Fabry-Pérot plasmonic cavity corresponds to $k_{\min} = 3$; the fundamental mode with $k = 0$ is beyond the accessible gate voltages. **b**, Examples of high-frequency potential distribution in the plasmon mode (real part) under resonant conditions for given k . Brown and blue colours represent positive and negative values of electrical potential, respectively. S,G and D stand for source, gate, and drain terminals, respectively. **c**, Experimental (symbols) and calculated (solid line) plasmon wavelengths λ_p as functions of carrier density, as obtained from (a). The corresponding value of the inverse compression ratio, λ_0/λ_p , for $f = 2 \text{ THz}$ is given on the right axis. **d**, Plasmon lifetime τ_p and quality factor Q as obtained from the width of the resonances shown in (e). Error bars stem from the fitting procedure. **e**, Experimental and calculated responsivities as functions of $V_g^{-1/2}$, normalized to the effective antenna impedance $Z = V_a^2/P$ relating the incident power to the resulting gate-to-channel voltage V_a . The theoretical Dyakonov-Shur dependence was obtained by using characteristic $\tau_p = 0.6 \text{ ps}$ from (d). Inset: normalized responsivity R_a/Z after the subtraction of a smooth non-oscillating background. The solid blue line is the best Lorentzian fit to the data, with $\delta = 0.1 \text{ V}^{-1/2}$, which translates to $\tau_p = 0.5 \text{ ps}$.

ular, we have found that at $f = 460 \text{ GHz}$, the resonances are already well-developed (Supplementary Fig. 4). At such low f , only two peaks in the photoresponse (one for electrons and one for holes) are observed for the same gate voltage span as in Fig. 2b along with an apparent increase of their full width at half-height. These observations are in full agreement with the plasmon-assisted photodetection model discussed below.

Plasmon resonances in graphene FETs

We argue that the observed peaks in the photoresponse emerge as a result of plasmon resonance in the FET channel. To this end, we model our FET as a plasmonic Fabry-Perot cavity endowed with a rectifying element.

This results in responsivity given by

$$R_a = \frac{R_0}{|1 - r_s r_d e^{2iqL}|^2}, \quad (1)$$

where R_0 is a smooth function of carrier density n and frequency f that depends on the microscopic rectification mechanism, r_s and r_d are the wave reflection coefficients from the source and drain terminals, respectively, and q is the complex wave vector governing the wave propagation in the channel (Supplementary Note 5). In gated 2D electron systems, the relation between the frequency ω and the real part of the wave vector q' is linear, $\omega = sq'$, where the plasmon phase velocity is

$$s = v_F \sqrt{4\alpha_c k_F d} = \sqrt{\frac{e}{m} |V_g|}. \quad (2)$$

Here m and e are the effective mass of carriers and the elementary charge respectively, v_F and $k_F = \sqrt{\pi n}$ are the Fermi velocity and the Fermi wave vector, d is the distance to the gate, $\alpha_c = e^2/(4\pi\epsilon_z\epsilon_0\hbar v_F)$ is the dimensionless coupling constant and ϵ_z is the out-of-plane dielectric permittivity^{33,34}. We further note that eq. (2) is valid for monolayer graphene upon replacement of the effective mass m with the cyclotron mass, $m \rightarrow \hbar k_F/v_F$ (see Supporting Note 6). The latter increases with gate-induced carrier density n , thereby limiting the tuning range of s for a given voltage span. In contrast, in the case of BLG, m is nearly constant ($\approx 0.036m_e$) for experimentally accessible values of V_g , a feature that allows us to vary s over a wider range and thus switch the detector between multiple modes, as we now proceed to show.

It follows from eq. (1), that the responsivity of our Fabry-Perot rectifier is expected to peak whenever the denominator in eq. (1) approaches zero. In our devices, the source potential is clamped to antenna voltage, and no ac current flows into the drain, therefore $r_s r_d \approx -1$ (Ref. 3, 32). The resonances should therefore occur whenever the real part of the wave number is quantized according to

$$q' = \frac{\pi}{2L}(2k+1), \quad k = 0, 1, 2, \dots \quad (3)$$

The quantization rule (3) combined with eq. (2) predicts a linear dependence of the mode number k on $|V_g|^{-1/2}$ which may serve as a benchmark for plasmon resonances in the FET channel. This is indeed the case of our photodetector, as shown in Figs. 3a,e and Supplementary Fig. 3c. The slope of the experimental $k(|V_g|^{-1/2})$ dependence in Fig. 3a matches well the theoretical expectation for a BLG Fabry-Perot cavity of length $L = 6 \mu\text{m}$. At large $|V_g|^{-1/2}$, we find a slight upward trend in the experimental data with respect to the linear dependence. We attribute this trend to deviations of the plasmon dispersion from the linear law at short wavelengths which stem from the non-local relation between electric potential and carrier density³³. Note that the known non-parabolicity of the BLG spectrum³⁵ resulting in an increase of m at large density n would bend the dependence in Fig. 3a in the opposite direction.

Photovoltage-based spectroscopy of 2D plasmons

The resonant gate-tunable response of our detectors offers a convenient tool to characterize plasmon modes in graphene channels. From eq. (3) it follows that resonances occur if $L = (2k+1)\lambda_p/4$, where $\lambda_p = 2\pi/q'$ is the plasmon wavelength (Fig. 3b). Using the experimentally observed peak positions, we have determined the density dependence of λ_p , shown in Fig. 3c, which flaunts excellent agreement with theory. The compression ratio λ_p/λ_0 between the plasmon and free-space wavelength ($\lambda_0 = c/f$ and c the speed of light in vacuum) ranges between 1/50 and 1/150, highlighting the ultra-strong confinement of THz fields enabled by graphene plasmons, matching the record value known in the literature²⁰.

Apart from λ_p , the resonant responsivity carries information about another valuable characteristic of plasmons, namely, their lifetime, τ_p . The latter is related to the peak width at half-height δ via (Supplementary Note 7)

$$V_g^{-1/2}/\delta = \omega\tau_p. \quad (4)$$

Using Lorentzian fits to the photoresponse curves (inset of Fig. 3e), we have extracted τ_p as a function of n , shown in Fig. 3d. The lifetime was found to range between ≈ 0.3 and ≈ 0.9 ps, which is slightly shorter than the transport time $\tau_{tr} \approx 2$ ps as extracted from the mobility, $\tau_{tr} = m\mu/e$ (Supplementary Note 1). The corresponding quality factor, $Q = 2\pi f\tau_p$, was found to vary between 4 and 11 for $f = 2$ THz, and between 0.2 and 0.7 for $f = 0.13$ THz, see Fig. 3d. The latter implies that it is unreasonable to expect resonant photoresponse of such detectors in the GHz range, and they can only operate in the broadband (non-resonant) regime, in accordance with the data in Fig. 2a. On the contrary, the resonant responsivity should become more profound at higher frequencies of the THz window and can be further enhanced in graphene FETs of higher quality, such as those using graphite gates to screen remote charge impurities³⁶.

Miniband plasmons in graphene/hBN superlattices

The approach demonstrated above is universal and can be applied to studies of plasmons in arbitrary high-mobility 2D systems embedded in FET channels, as we now proceed to show for the case of devices made of BLG/hBN moiré superlattices³⁷.

Figures 4b and Supplementary Fig. 3c show examples of R_a as a function of V_g recorded in our superlattice devices in response to 2 THz radiation. As in the case of plain BLG, the overall evolution of the superlattice responsivity $R_a(V_g)$ follows that of the FET-factor (black curve) modulated by the plasmon resonances. Note the total number of resonances is smaller due to the shorter FET channel (cf. Supplementary Fig. 3c) and they are visible only for $V_g < 0$, presumably due to a stronger non-linearity in this detector for negative doping (in another superlattice FET, the resonances were well-observed for both V_g polarities as shown in Supplementary Fig. 3c). Importantly, the FET-factor in these devices is, in turn, a more complex function of V_g (cf. inset of Fig. 2a) due to the presence of secondary neutrality points (sNP) stemming from a peculiar band structure of the BLG/hBN superlattice. The latter is characterized by narrow minibands emerging in the vicinity of the \tilde{K}/\tilde{K}' -points of the superlattice Brillouin zone³⁷ (Fig. 4c). The sNPs are clearly visible as peaks in the FET resistance which appear around $V_g = \pm 10$ V (Fig. 4a).

A striking feature of the superlattice photoresponse is the resonances appearing when the Fermi level is brought close to the sNP (pink arrows in Fig. 4b). The resonances are of opposite sign with respect to those observed near the main NP (blue arrows), which indicates that they

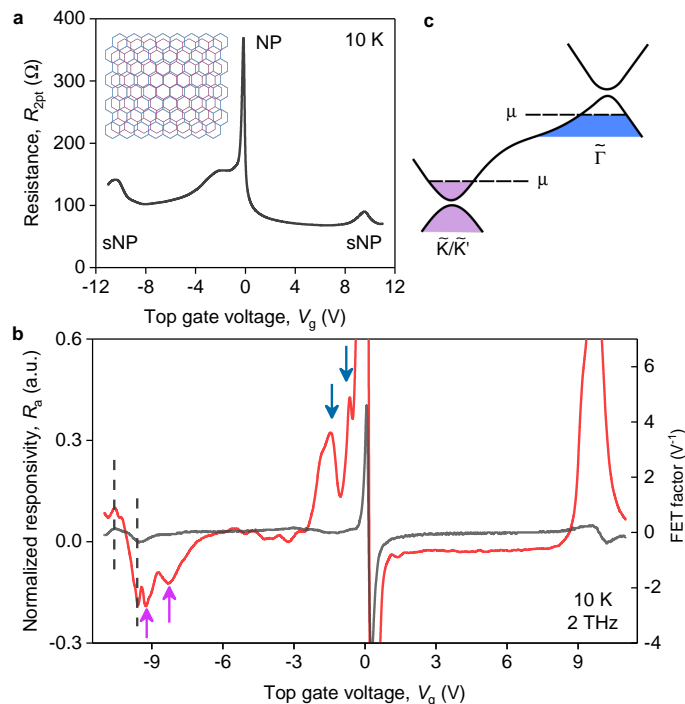


FIG. 4. **Miniband plasmons in BLG/hBN moiré superlattices.** **a**, Two-terminal resistance of one of our BLG/hBN superlattice devices as a function of V_g measured at given T . Inset: Illustration of the BLG/hBN superlattice demonstrating a mismatch between graphene and hBN lattice constants. For simplicity, only one graphene layer is shown. **b**, Normalized responsivity (red) and the FET-factor (black) as a function of V_g measured in the same device as in (a). Dashed line's trace V_g where the FET-factor reaches extreme values in the vicinity of the sNP. Pink (blue) arrows point to the resonant peaks near the secondary (main) NP. $L = 3 \mu\text{m}$. **c**, Schematic representation of the BLG/hBN superlattice band structure. In the vicinity of the $\bar{\Gamma}$ -point (blue), BLG supports propagation of the ordinary plasma waves. Miniband THz plasmons emerge when the chemical potential approaches the sNP (pink).

originate from the plasmons supported by the charge carriers of the opposite type (cf. Fig. 2b). Since the latter are hosted by the minibands near the \tilde{K}/\tilde{K}' -points of the superlattice Brillouin zone (Fig. 4c), our measurements provide evidence for miniband plasmons that were long identified theoretically³⁸ but remained elusive in experiment. To date, the experimental studies of superlattice plasmons have been only performed at room temperature using scattering-type scanning near field microscopy operating in the mid-IR domain³⁹. The mid-IR excitation energy ($10 \mu\text{m} \approx 120 \text{ meV}$) is high enough to induce interband absorption close to the sNP, which hampers the observation of plasmons in superlattice minibands³⁹. In contrast, our approach relies on the low-energy excitations ($2 \text{ THz} \approx 8 \text{ meV}$), is applicable at cryogenic temperatures, and, therefore, paves a convenient way for further studies of miniband plasmonics.

DISCUSSION

Resonant responsivity is a universal phenomenon in ultra-clean graphene devices and is expected to be independent of the physical mechanisms behind the rectification of the ac field into a dc photovoltage. Nevertheless, it is important to establish possible nonlinearities responsible for the rectification, for example, in order to be able

to increase the magnitude of responsivity.

We first note that the aforementioned asymmetry in $R_a(V_g)$ between electron and hole doping indicates rectification at the p - n junction formed in vicinity of the contacts. This rectification usually appears due to the thermoelectric effect arising as a result of non-uniform sample heating and the difference between the Seebeck coefficients in the graphene channel and contact regions^{21,24,32,40} (Supplementary Note 8). However, R_a remains finite even for $V_g > 0$, where both channel and contact areas are n -doped. This indicates that alternative rectification mechanisms are also involved.

Another commonly accepted mechanism is the rectification arising as a result of the simultaneous action of longitudinal high-frequency field and modulation of channel conductivity, also known as resistive self-mixing². The latter can be enhanced by the dc photovoltage that balances the difference between electron kinetic energies at the source and drain terminals^{2,3}, similar to Bernoulli's law for classical fluids. Both mechanisms are combined into so-called Dyakonov- Shur (DS) rectification³ and result in R_0 proportional to the sensitivity of the conductivity to the gate voltage variation⁴, given by the F -factor introduced above (Supplementary Note 9). In Fig. 3e we compare the resonant photoresponse of our

BLG photodetector with the responsivity expected from the DS model³ assuming an average $\tau_p \sim 0.6$ ps, as found from Fig. 3d, and using the effective antenna impedance Z as the only fitting parameter. The two curves show the same functional behaviour and match quantitatively for the n-doped case (where the p-n junction is absent) and $Z \approx 74 \Omega$, a value close to that expected from the equivalent circuit design³². We further note, that although the original DS proposal was based on the hydrodynamic electron transport^{41,42}, an identical photoresponse is expected outside the hydrodynamic window as it follows from the analysis of graphene's nonlinear conductivity⁴³.

Last but not least, we note that while the overall trend of the responsivity is well-described by the model introduced above, the values of τ_p extracted from the peak width at half-height are found to be below the momentum relaxation time. This suggests that other mechanisms of resonance broadening are also involved. In particular, leakage of plasma waves into metal contacts⁴⁴ and electromagnetic dissipation in antenna may also contribute to the apparent resonance width. We have found that respective contributions to τ_p^{-1} are most pronounced at large carrier densities and small harmonic numbers (Supplementary Figs. 6 and 7), in agreement with experimental data in Fig. 3d. Elimination of these damping channels, e.g. with Schottky/tunnel contacts and low-impedance antennas, may extend the resonant detection down to tens of gigahertz⁴⁵. Other dissipation channels such as electron viscosity^{46,47} and interband absorption¹⁸ should be most pronounced at higher-order harmonics and in the vicinity of the NP, as opposed to the data in Fig. 3d, and are unlikely relevant to the present study.

In conclusion, we have shown that high-mobility graphene FETs exploiting far-field coupling to incoming radiation can operate as resonant THz photodetectors. In addition to their potential applications in high-responsivity detection and on-chip spectroscopy of the THz radiation, our devices also represent a convenient tool to study plasmons under conditions where other approaches may be technically challenging. Due to their compact size and far-field coupling, our photodetectors can easily be employed to carry out plasmonic experiments in extreme cryogenic environments and in strong magnetic fields, as well in studies of more complex van der Waals heterostructures. As an example, we have demonstrated the use of our approach to reveal low-energy plasmons hosted by moiré minibands in BLG/hBN superlattices. The method has a strong potential for studies of collective modes in magnetic minibands which have recently gained a great level of attention⁴⁸.

METHODS

Device fabrication

All our devices were made of BLG. BLG was first encapsulated between relatively thick hBN crystals using the standard dry-peel technique³⁰. The thickness of the

top hBN was measured by atomic force microscopy. The stack was then deposited either directly on top of a low-conductivity boron-doped silicon wafer capped with a thin oxide layer (500 nm) or on a predefined back gate electrode. The resulting van der Waals heterostructure was patterned using electron beam lithography to define contact regions. Reactive ion etching was then used to selectively remove the areas unprotected by a lithographic mask, resulting in trenches for depositing electrical leads. Metal contacts to graphene were made by evaporating 3 nm of Cr and 60 nm of Au. Afterwards, a second e-beam lithography was used to design the top gate. The graphene channel was finally defined by a third round of e-beam lithography, followed by reactive ion etching using Poly(methyl methacrylate) and gold top gate as the etching mask. Finally, we used optical photolithography to pattern large antenna (spiral or bow-tie) sleeves connected to the source and the top-gate terminals, followed by evaporation of 3 nm of Cr and 400 nm of Au. Antennas were designed to operate at an experimentally accessible frequency range.

Photoresponse measurements

Photoresponse measurements were performed in a variable temperature optical cryostat equipped with a polyethylene window that allowed us to couple the photodetector to incident THz radiation. The latter was focused to the device antenna by a silicon hemispherical lens attached the silicon side of the chip (Fig. 1b). The transparency of the chips to THz radiation over the entire temperature and frequency range was verified in transmission experiments using a home-made optical cryostat coupled to the THz spectrometer. Photovoltage measurements were performed using either a standard lockin amplifier synchronized with a chopper rotating at 1 kHz frequency, positioned between the radiation source and the cryostat window, or by a home-made measurement board.

In order to study the photoresponse of our detectors at different frequencies, we used three radiation sources. Sub-THz radiation was provided by two backward wave oscillators (BWO) generating $f = 0.13$ THz and $f = 0.46$ THz. For higher frequencies, a quantum cascade continuous wave laser based on a GaAs/Al_{0.1}Ga_{0.9}As heterostructure emitting $f = 2.026$ THz radiation was used.

The responsivity of our devices was calculated assuming that the full power delivered to the device antenna funnelled into the FET channel. The as-determined value provides the lower bound for our detectors' responsivity and is usually referred to as extrinsic. The calculation procedure consisted of a few steps. First the source-to-drain voltage U_{dark} was measured as a function of V_g in the dark. Then, the dependence of the source-to-drain voltage U_{SD} on V_g was recorded under illumination with THz radiation. The difference $\Delta U = U_{\text{SD}} - U_{\text{dark}}$ formed the photovoltage. At the next stage, we measured the full power P_{full} delivered to the cryostat window using Golay cell. The responsivity was then calculated as

$R_a = \Delta U/P$, where $P \approx P_{\text{full}}/3.5$ is the power delivered to the device antenna after accounting for losses in the silicon lens and the cryostat optical window (≈ 5.5 dB). All the measurements reported above were performed in the linear-in- P regime. The performance of our detectors outside the linear regime is discussed in Supplementary Note 10 and reported in Supplementary Fig. 8.

Data availability

The data that support the findings of this study are available from the corresponding author upon reasonable request.

Acknowledgements

Device fabrication and Manchester's part of the work was supported by the European Research Council, the Graphene Flagship and Lloyds Register Foundation. The work at the MSPU (Photoresponse measurements) has been carried out with the support of the Russian Science Foundation (project No. 17-72-30036). D.A.B. acknowledges financial support from Leverhulme Trust. Experimental work of M.M. (transport measurements) was supported by Russian Science Foundation (Grant 18-72-00234). M.P. is supported by the European Unions Horizon 2020 research and innovation programme under grant agreement No. 785219 - GrapheneCore2. Modelling of antenna electrostatics was supported by RFBR (Project 18-29-20116). Theoretical work of D.S. was supported by the grant 16-19-10557 of the Russian Science Foundation. Photoresponse measurements have been performed using quantum cascade laser fabricated by A. Valavanis in the group of Prof. Dragan Indjin in the University of Leeds (UK). We thank A. Tomadin, R. Krishna Kumar, A. Berdyugin, L. Levitov and V. Fal'ko for fruitful discussions.

Author contributions

D.A.B. and G.F. designed and supervised the project. S.G.X. and I.G. fabricated the devices. Photoresponse measurements were carried out by I.G., M.M and D.A.B. Data analysis was performed by D.A.B. and D.S. Theory analysis was done by D.S. The manuscript was written by D.A.B. and D.S. with input from I.V.G., M.P., A.P. and A.K.G. Experimental support was provided by I.T., D. Y., S.Z. and G.G. T.T. and K.W. grew the hBN crystals. All authors contributed to discussions.

Competing interests

The authors declare no competing interests.

- ¹Dhillon, S. S. *et al.* The 2017 terahertz science and technology roadmap. *Journal of Physics D: Applied Physics* **50**, 043001 (2017).
- ²Daryoosh, S. *Handbook of terahertz technology for imaging, sensing and communications* Woodhead Publishing (2013).
- ³Dyakonov, M. & Shur, M. Detection, mixing, and frequency multiplication of terahertz radiation by two-dimensional electronic fluid. *IEEE Transactions on Electron Devices* **43**, 380–387 (1996).

- ⁴Knap, W. *et al.* Field effect transistors for terahertz detection: Physics and first imaging applications. *Journal of Infrared, Millimeter, and Terahertz Waves* **30**, 1319–1337 (2009).
- ⁵Vicarelli, L. *et al.* Graphene field-effect transistors as room-temperature terahertz detectors. *Nature Materials* **11**, 865–871 (2012).
- ⁶Spirito, D. *et al.* High performance bilayer-graphene Terahertz detectors. *Applied Physics Letters* **104**, 061111 (2014).
- ⁷Tong, J., Muthee, M., Chen, S. Y., Yngvesson, S. K. & Yan, J. Antenna Enhanced Graphene THz Emitter and Detector. *Nano Letters* **15**, 5295–5301 (2015).
- ⁸Qin, H. *et al.* Room-temperature, low-impedance and high-sensitivity terahertz direct detector based on bilayer graphene field-effect transistor. *Carbon* **116**, 760–765 (2017).
- ⁹Generalov, A. A., Andersson, M. A., Yang, X., Vorobiev, A. & Stake, J. A 400-GHz Graphene FET Detector. *IEEE Transactions on Terahertz Science and Technology* **7**, 614–616 (2017).
- ¹⁰Peralta, X. G. *et al.* Terahertz photoconductivity and plasmon modes in double-quantum-well field-effect transistors. *Appl. Phys. Lett.* **81**, 1627–1629 (2002).
- ¹¹Knap, W., Deng, Y., Romyantsev, S. & Shur, M. S. Resonant detection of subterahertz and terahertz radiation by plasma waves in submicron field-effect transistors. *Appl. Phys. Lett.* **81**, 4637–4639 (2002).
- ¹²Tepe, F. *et al.* Room-temperature plasma waves resonant detection of sub-terahertz radiation by nanometer field-effect transistor. *Applied Physics Letters* **87**, 85–88 (2005).
- ¹³Muravev, V. M. & Kukushkin, I. V. Plasmonic detector/spectrometer of subterahertz radiation based on two-dimensional electron system with embedded defect. *Appl. Phys. Lett.* **100**, 082102 (2012).
- ¹⁴Giliberti, V. *et al.* Downconversion of terahertz radiation due to intrinsic hydrodynamic nonlinearity of a two-dimensional electron plasma. *Physical Review B* **91**, 165313 (2015).
- ¹⁵Ju, L. *et al.* Graphene plasmonics for tunable terahertz metamaterials. *Nature Nanotechnology* **6**, 630–634 (2011).
- ¹⁶Yan, H. *et al.* Tunable infrared plasmonic devices using graphene/insulator stacks. *Nature Nanotechnology* **7**, 330–334 (2012).
- ¹⁷Fei, Z. *et al.* Gate-tuning of graphene plasmons revealed by infrared nano-imaging. *Nature* **486**, 82–85 (2012).
- ¹⁸Chen, J. *et al.* Optical nano-imaging of gate-tunable graphene plasmons. *Nature* **487**, 77–81 (2012).
- ¹⁹Grigorenko, A., Polini, M. & Novoselov, K. Graphene plasmonics. *Nature Photonics* **6**, 749–758 (2012).
- ²⁰Woessner, A. *et al.* Highly confined low-loss plasmons in graphene-boron nitride heterostructures. *Nature Materials* **14**, 421–425 (2015).
- ²¹Alonso-González, P. *et al.* Acoustic terahertz graphene plasmons revealed by photocurrent nanoscopy. *Nature Nanotechnology* **12**, 31–36 (2016).
- ²²Ni, G. *et al.* Fundamental limits to graphene plasmonics. *Nature* **557**, 530–533 (2018).
- ²³Koppens, F. H. L. *et al.* Photodetectors based on graphene, other two-dimensional materials and hybrid systems. *Nature Nanotechnology* **9**, 780–793 (2014).
- ²⁴Cai, X. *et al.* Sensitive room-temperature terahertz detection via the photothermoelectric effect in graphene. *Nature Nanotechnology* **9**, 814–819 (2014).
- ²⁵Auton, G. *et al.* Terahertz Detection and Imaging Using Graphene Ballistic Rectifiers. *Nano Letters* **17**, 7015–7020 (2017).
- ²⁶Otsuji, T., Hanabe, M., Nishimura, T. & Sano, E. A grating-bicoupled plasma-wave photomixer with resonant-cavity enhanced structure. *Optics express* **14**, 4815–4825 (2006).
- ²⁷Tomadin, A., Tredicucci, A., Pellegrini, V., Vitiello, M. S. & Polini, M. Photocurrent-based detection of terahertz radiation in graphene. *Applied Physics Letters* **103**, 211120 (2013).
- ²⁸Ryzhii, V., Otsuji, T., Ryzhii, M. & Shur, M. S. Double graphene-layer plasma resonances terahertz detector. *J. Phys.*

- D: Appl. Phys.* **45**, 302001 (2012).
- ²⁹Fateev, D. V., Mashinsky, K. V. & Popov, V. V. Terahertz plasmonic rectification in a spatially periodic graphene. *Appl. Phys. Lett.* **110**, 061106 (2017).
- ³⁰Kretinin, A. V. *et al.* Electronic properties of graphene encapsulated with different two-dimensional atomic crystals. *Nano Letters* **14**, 3270–3276 (2014).
- ³¹Ryzhii, V. & Shur, M. S. Resonant terahertz detector utilizing plasma oscillations in two-dimensional electron system with lateral schottky junction. *Jpn. J. Appl. Phys.* **45**, L1118 (2006).
- ³²Bandurin, D. A. *et al.* Dual origin of room temperature sub-terahertz photoresponse in graphene field effect transistors. *Applied Physics Letters* **112**, 141101 (2018).
- ³³Chaplik, A. Possible crystallization of charge carriers in low-density inversion layers. *Sov. Phys. JETP* **35**, 395 (1972).
- ³⁴Tomadin, A. & Polini, M. Theory of the plasma-wave photoreponse of a gated graphene sheet. *Phys. Rev. B* **88**, 205426 (2013).
- ³⁵Zou, K., Hong, X. & Zhu, J. Effective mass of electrons and holes in bilayer graphene: Electron-hole asymmetry and electron-electron interaction. *Phys. Rev. B* **84**, 085408 (2011).
- ³⁶Zibrov, A. A. *et al.* Tunable interacting composite fermion phases in a half-filled bilayer-graphene Landau level. *Nature* **549**, 360–364 (2017).
- ³⁷Mucha-Kruczynski, M., Wallbank, J. & FalKo, V. Heterostructures of bilayer graphene and h-BN: Interplay between misalignment, interlayer asymmetry, and trigonal warping. *Phys. Rev. B* **90**, 205418 (2013).
- ³⁸Tomadin, A., Guinea, F. & Polini, M. Generation and morphing of plasmons in graphene superlattices. *Phys. Rev. B* **90**, 161406(R) (2014).
- ³⁹Ni, G. *et al.* Plasmons in graphene moiré superlattices. *Nature Materials* **14**, 1217–1222 (2015).
- ⁴⁰Jung, M., Rickhaus, P., Zihlmann, S., Makk, P. & Schonenberger, C. Microwave Photodetection in an Ultraclean Suspended Bilayer Graphene p-n Junction. *Nano Letters* **16**, 6988–6993 (2016).
- ⁴¹Bandurin, D. *et al.* Fluidity onset in graphene. *Nature Communications* **9**, 4533 (2018).
- ⁴²Berdyugin, A. *et al.* Measuring Hall Viscosity of Graphene’s Electron Fluid. *arXiv:1806.01606* (2018).
- ⁴³Principi, A., Bandurin, D., Rostami, H. & Polini, M. Pseudo-Euler equations from nonlinear optics: plasmon-assisted photodetection beyond hydrodynamics. *arXiv:1811.06540* (2018).
- ⁴⁴Satou, A., Ryzhii, V., Mitin, V. & Vagidov, N. Damping of plasma waves in two-dimensional electron systems due to contacts. *Physica Status Solidi (B)* **246**, 2146–2149 (2009).
- ⁴⁵Graef, H. *et al.* Ultra-long wavelength Dirac plasmons in graphene capacitors. *J. Phys. Mater.* 01LT02 (2018).
- ⁴⁶Kumar, R. K. *et al.* Superballistic flow of viscous electron fluid through graphene constrictions. *Nature Physics* **13**, 1182–1185 (2017).
- ⁴⁷Svintsov, D. Hydrodynamic-to-ballistic crossover in dirac materials. *Phys. Rev. B* **97**, 121405 (2018).
- ⁴⁸Krishna Kumar, R. *et al.* High-temperature quantum oscillations caused by recurring Bloch states in graphene superlattices. *Science* **357**, 181–184 (2017).
- ⁴⁹Aizin, G. R. & Dyer, G. C. Transmission line theory of collective plasma excitations in periodic two-dimensional electron systems: Finite plasmonic crystals and tamm states. *Phys. Rev. B* **86**, 235316 (2012).
- ⁵⁰Dyer, G. C. *et al.* Induced transparency by coupling of tamm and defect states in tunable terahertz plasmonic crystals. *Nature Photonics* **7**, 925 (2013).
- ⁵¹Collin, R. E. *Field theory of guided waves* (McGraw-Hill, 1960).
- ⁵²Das Sarma, S., Adam, S., Hwang, E. H. & Rossi, E. Electronic transport in two-dimensional graphene. *Rev. Mod. Phys.* **83**, 407–470 (2011).
- ⁵³Low, T., Perebeinos, V., Kim, R., Freitag, M. & Avouris, P. Cooling of photoexcited carriers in graphene by internal and substrate phonons. *Phys. Rev. B* **86**, 045413 (2012).

Supplementary Note 1: Device characterization

Our photodetectors represent two-terminal field-effect transistors (FET) and, therefore, the measured conductance (Fig. 1d of the main text), which contains non-zero contribution from the BLG-metal contact, does not provide the information on the quality of the FET channel. In order to estimate the mobility of charge carriers in the BLG channel, we fabricated a reference multi-terminal Hall bar using the same procedure as described in Methods. The Hall bar was characterized using the standard four-terminal geometry that involved the measurements of its sheet resistance ρ as a function of carrier density n and temperature T (Supplementary Fig. 1). One can see a typical field-effect behavior for high-quality graphene that manifests itself in sharp peak in ρ at the charge neutrality point which decays steeply with increasing n . The charge carrier mobility μ was calculated using the Drude formula, $\mu = \sigma/ne$, and for typical $n = 10^{12} \text{ cm}^{-2}$ exceeded $10 \text{ m}^2/\text{Vs}$ at liquid helium T and remained around $2.5 \text{ m}^2/\text{Vs}$ at room temperature.

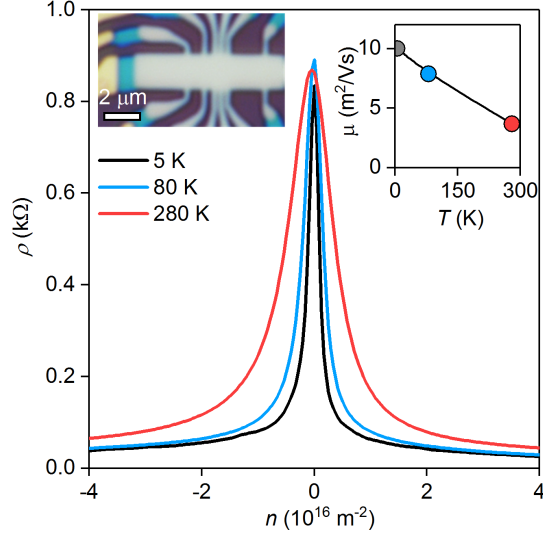


FIG. 1. **Reference multiterminal BLG field effect transistor.** Sheet resistance as a function of n for different T measured in the standard four-terminal geometry. Left inset: Optical photographs of our reference Hall bar. Right inset: Mobility as a function of T measured at $n = 10^{12} \text{ cm}^{-2}$.

Supplementary Note 2: High-responsivity THz detection in dual-gated BLG field effect transistors

As discussed in the main text, the responsivity of the THz detectors made of the field effect transistors is proportional to the sensitivity of the FET conductivity to the gate voltage variation. To improve the performance of our detectors, we took advantage of BLG's gate-tunable band structure and fabricated a dual-gated device (top and bottom insets of Supplementary Fig. 2a). The idea is that when an electric field is applied perpendicular to the channel it induces a band gap in BLG that leads to a steeper dependence of the FET resistance $R_{2\text{pt}}$ on the gate voltage. Supplementary Fig. 2a shows examples of $R_{2\text{pt}}(V_{\text{tg}})$ dependences measured at few V_{bg} demonstrating the expected increase of $R_{2\text{pt}}$ with increasing the average displacement field $D = \frac{\epsilon}{2}(V_{\text{tg}}/d_{\text{bg}} - V_{\text{bg}}/d_{\text{tg}})$ applied to BLG, where d_{bg} (d_{tg}) is the thickness of the bottom (top) hBN crystal and ϵ is its dielectric constant.

Supplementary Fig. 2b shows the top gate voltage dependence of R_a measured in response to 0.13 THz radiation in the dual-gated detector. In the case of zero back gate voltage (black curve), $R_a(V_{\text{tg}})$ repeats the behaviour of another detector reported in Fig. 2a of the main text. Namely, the responsivity reaches its maximum of about 200 V/W near the NP where it flips its sign because of the change in the charge carrier type. Note, the absolute value of the maximum responsivity is very close to that reported in the main text (Fig. 2b) highlighting the reproducibility of our detectors' performance. When the back gate voltage is applied, the responsivity increases drastically (red and blue curves in Supplementary Fig. 2b). Already for a moderate $D \sim 0.1 \text{ V/nm}$ the responsivity increases by more than an order of magnitude and exceeds 3 kV/W. The corresponding noise equivalent power, estimated using the Johnson-Nyquist noise spectral density for the same D , reaches 0.2 pW/Hz^{1/2}. This makes our detector competitive not only with other graphene-based THz detectors²³ but also with some commercial semiconductor and superconductor bolometers (Table 1).

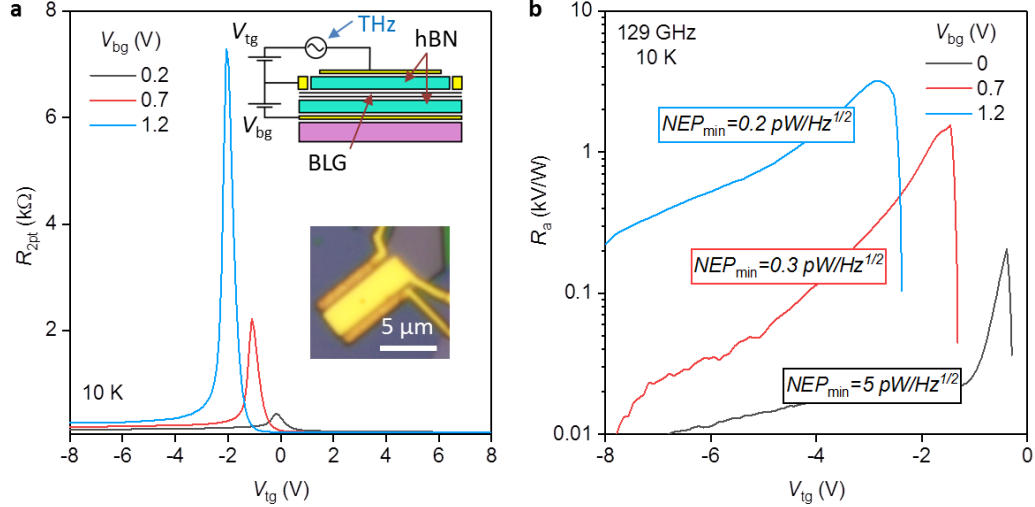


FIG. 2. **Photoresponse of a dual-gated BLG detector.** **a**, Two-terminal resistance as a function of V_{tg} measured in a dual-gated BLG FET for different V_{bg} . Top inset: Schematic of a dual-gated THz detector. Bottom inset: Optical photographs of the device. **b**, Responsivity as a function of V_{tg} for different V_{bg} measured at given f and T .

Detector	NEP, $\text{pW}/\text{Hz}^{0.5}$	Operation Temperature, K	Reference
Superconducting hot electron bolometer*	0.1 - 1	2.5 - 4.5	www.boselec.com www.scontel.ru
Semiconductor hot electron bolometer (e.g. InSb)	0.04 - 0.8	1.6 - 4.2	www.infraredlaboratories.com
Dual-gated bilayer graphene THz detector	0.2	10	This work

TABLE 1. **Comparison of cryogenic THz detectors.** *Reported values of NEP were taken for the same frequency (0.13 THz) used to probe our dual-gated devices.

Supplementary Note 3: Further examples of resonant photoresponse

To illustrate that the observed resonant photoresponse is reproducible for different electronic systems embedded in FETs of various lengths L and coupled to different antennas, Supplementary Fig. 3c shows another example of the photovoltage $\Delta U(V_g)$ emerging when the incoming 2 THz radiation is coupled to the broadband logarithmic spiral antenna connected to another FET. The latter is made of BLG having its crystallographic axis aligned with those of hBN, that reveals itself in peculiar three-peaks $R(V_g)$ structure, shown in Supplementary Fig. 3e. The photoresponse curves are rather similar to those shown in Supplementary Fig. 2b of the main text, namely they follow the envelope trend set by the FET-factor $F = -\frac{1}{\sigma} \frac{d\sigma}{dV_g}$ (Supplementary Fig. 3d) superimposed with the resonant peaks. The resonances are periodic in $V_g^{-1/2}$ (inset to Supplementary Fig. 3c) and are clearly seen for both electron and hole doping. Importantly, on the contrary to Fig. 2b, the photoresponse now changes sign multiple times following non-trivial $F(V_g)$ evolution.

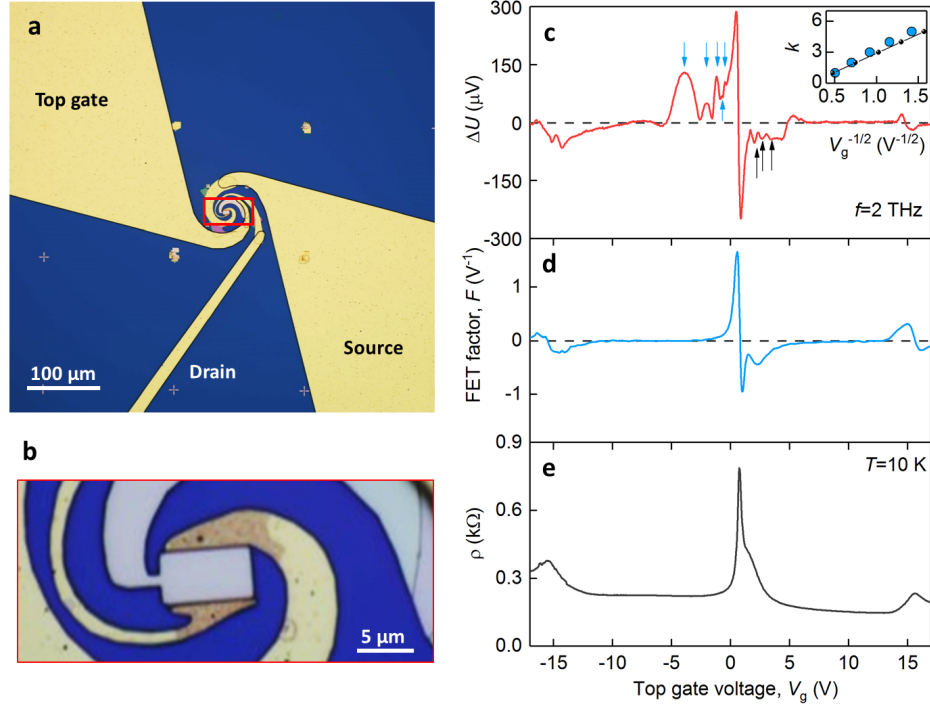


FIG. 3. **Further examples of resonant photoresponse.** **a-b**, Optical photographs of another THz photodetector. FET channel is coupled to incoming radiation by a broadband logarithmic spiral antenna. The red rectangle in (a) indicates the region shown in (b). **c**, Photovoltage versus V_g recorded as a response to $f = 2$ THz radiation in one of our BLG/hBN superlattice devices. Arrows point to the resonant peaks. Inset: Mode number k as a function of $V_g^{-1/2}$ taken from the peaks marked by the blue arrows. Black: theoretical dependence expected for $L = 4 \mu\text{m}$, $m = 0.036me$ and $r_s r_d = -1$. **d**, FET-factor F as a function of V_g obtained from the data in (a). **e**, Resistivity as a function of V_g for the device in (a-b) measured at $T = 10$ K. Three peaks correspond to the secondary neutrality points of BLG/hBN superlattice.

Supplementary Note 4: Resonant detection of sub-THz radiation

We have also studied the performance of our detectors at frequencies intermediate to those reported in Figs. 2a and b of the main text and found that the resonant operation onsets already in the middle of the sub-THz domain. Figure 4 shows the gate voltage dependence of R_a recorded in response to 460 GHz radiation. In the vicinity of the charge neutrality point (NP) the responsivity peaks and changes its sign in agreement with the evolution of the FET-factor with the gate voltage (black curve in Supplementary Fig. 4) as discussed in the main text. However, away from the NP the responsivity peaks for both electron and hole doping (stars in Supplementary Fig. 4) despite the fact that $F(V_g)$ is featureless. These peaks stem from the plasmon resonances in the FET channel as it follows from the comparison of the experimental data with theory (inset of Supplementary Fig. 4). In good agreement with theory, at lower frequencies the number of resonant modes, which can be observed for the same gate voltage span, is smaller compared to that found at 2 THz (Fig. 2b of the main text). In addition, the resonances appear much broader than those observed at 2 THz (Fig. 2b) which is consistent with the reduced quality factor at sub-THz frequencies.

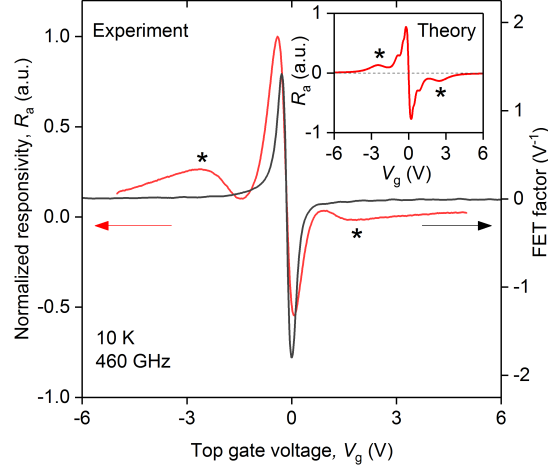


FIG. 4. **Resonant detection in the sub-THz domain.** Normalized to unity R_a as a function of V_g measured in response to 460 GHz radiation. Data is acquired on the same device as in Fig. 2 of the main text. Two resonances are clearly visible for electron and hole doping and marked by the black stars. Black curve: FET-factor as a function of V_{tg} . Inset: Theory for $L = 6 \mu\text{m}$, $f = 460 \text{ GHz}$, $m^* = 0.036m_e$, $T = 10 \text{ K}$ and $\tau = 0.6 \text{ ps}$ (eq. 38).

Supplementary Note 5: Fabri-Perot cavity model for plasmonic field-effect transistor

Gated two-dimensional electronic systems support plasma waves with the dispersion relation³³

$$\omega(\omega + i\tau^{-1}) = \frac{n_0 e^2 q}{2m^* \varepsilon_0 \varepsilon} (1 - e^{-2qd}). \quad (1)$$

where ω and q are the plasmon wavelength and wave vector, respectively, τ is the momentum relaxation time, n_0 is the carrier density, m^* is the effective mass of charge carriers, d is the distance to the gate, ε is the dielectric permittivity, and ε_0 is the vacuum permittivity.

Confinement of a 2d channel by source and drain contacts quantizes the wave vector q and leads to emergence of discrete plasmon frequencies. The quantization conditions can be obtained by requiring the oscillating quantity (e.g. voltage V_ω) to return to its original value after the channel round trip:

$$V_\omega r_s r_d e^{2iqL} = V_\omega, \quad (2)$$

where r_s and r_d are the complex-valued reflection coefficients at the source and drain terminals, respectively. Therefore, eigen frequencies of bounded plasmons can be found from

$$1 - r_s r_d e^{2iqL} = 0. \quad (3)$$

To see that the latter dispersion relation indeed appears in the nonlinear response functions, we model the FET channel as a transmission line (TL) fed by antenna voltage $U_{1\omega} = V_a \cos \omega t$ at the source side^{49,50}. The antenna may have finite impedance Z_a which will be taken into account at the end of this section. The TL is terminated by load impedance Z_{gd} at the drain side, and by impedance Z_{gs} at the source side. In real device, these impedances are due

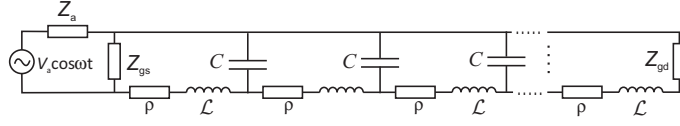


FIG. 5. **Transmission line equivalent circuit of gated 2d channel.** \mathcal{L} is the kinetic inductance of electrons, ρ is the channel resistivity, C is the effective gate-to-channel capacitance, and Z_{gd} is the load resistance at the drain side. All quantities are measured per unit length of the channel. $Z_{gd} \rightarrow \infty$ corresponds to Dyakonov-Shur boundary condition

to the capacitive coupling between the respective electrodes. The TL model is justified by the formal coincidence of TL equations (Telegrapher's equation) with transport equations in a gated FET channel.

The TL elements are specific inductance

$$\mathcal{L} = \frac{m^*}{n_0 e^2 W}, \quad (4)$$

capacitance per unit length

$$C = \frac{2W \epsilon \epsilon_0 q}{1 - e^{-2qd}}, \quad (5)$$

and resistance

$$\rho = \mathcal{L}/\tau, \quad (6)$$

where W is the channel width. It is readily seen that the dispersion relation for waves in an infinite transmission line⁵¹

$$q = \sqrt{C\mathcal{L}} \sqrt{\omega(\omega + \frac{i\rho}{\mathcal{L}})} \quad (7)$$

coincides with plasma wave dispersion (1) with proper values of line parameters (4-6). The characteristic (wave) impedance of transmission line is

$$Z_{tl} = \sqrt{\frac{\omega\mathcal{L} + i\rho}{\omega C}}. \quad (8)$$

A well-known result for current reflection coefficient from a loaded (drain) end of transmission line reads

$$r_d = \frac{Z_{tl} - Z_{gd}}{Z_{tl} + Z_{gd}}, \quad (9)$$

while for source end with fixed voltage

$$r_s = 1. \quad (10)$$

When the reflection coefficients and conditions at the ends of cavity are specified, it is straightforward to write down the solution for voltage across the TL (which is the gate-to-channel voltage in the actual FET):

$$V_\omega(x) = \frac{V_a}{2} \frac{e^{iqx} - r_s r_d e^{-iq(x-2L)}}{1 - r_s r_d e^{2iqL}}, \quad (11)$$

here r_d and r_s are given by Eqs. (9) and (10), respectively. The longitudinal electric field in the channel is given by

$$E_{x\omega} = \frac{qV_a}{2} \frac{e^{iqx} + r_s r_d e^{-iq(x-2L)}}{1 - r_s r_d e^{2iqL}}. \quad (12)$$

As the nonlinear response of the FET is proportional to the properly averaged square of ac electric field in the channel (12), it becomes apparent that responsivity would possess a plasma resonant factor $|1 - r_s r_d e^{2iqL}|^{-2}$, independent of the detection mechanism.

The account of finite antenna impedance results in a simple "renormalization" of input voltage in Eqs. (11) and (12):

$$V_a \rightarrow \frac{V_a}{1 + \frac{Z_a}{Z_{gs} \parallel Z_{tl, \text{in}}}}, \quad (13)$$

where \parallel stands for parallel connection of impedances, and $Z_{tl, \text{in}} = Z_{tl}(1 - r_d e^{2iqL}) / (1 + r_d e^{2iqL})$ is the input impedance of the transmission line (we have used $r_s = 1$). It is straightforward to show that the modification of input voltage can be translated in the modification of "resonant denominator"

$$1 - r_d e^{2iqL} \rightarrow (1 - r_d e^{2iqL}) \left[1 + \frac{Z_a}{Z_{gs}} \right] + (1 + r_d e^{2iqL}) \frac{Z_a}{Z_{tl}}. \quad (14)$$

The effect of Z_a in the square bracket is the reduction of input voltage due to the drop at internal antenna resistance. Finite value of Z_a in the second term leads to extra broadening or resonances, as analyzed below.

Supplementary Note 6: Gate tuning of graphene plasmons: monolayer vs bilayer

We briefly review the density dependences of plasmon frequencies in single layer graphene (SLG) and bilayer graphene (BLG). The general dispersion relation for gated plasmons in two-dimensional electron system with sheet conductivity σ reads³³

$$1 + \frac{iq\sigma}{2\omega\epsilon\epsilon_0}(1 - e^{-2qd}) = 0. \quad (15)$$

The study of plasmon dispersions in various two-dimensional systems is therefore reduced to evaluation of their frequency-dependent conductivity. In the classical ($\hbar\omega \ll \epsilon_F$) long-wavelength ($q \ll \omega/v_F$) limit, the latter is found from the Boltzmann equation⁵²

$$\sigma = \frac{e^2}{2} \int_0^{+\infty} d\varepsilon \rho(\varepsilon) \frac{v_p^2}{-i\omega + \tau_p^{-1}} \left(-\frac{\partial f_0}{\partial \varepsilon} \right), \quad (16)$$

where $\rho(\varepsilon)$ is the density of states, v_p is the velocity of carrier with momentum p , and f_0 is the equilibrium distribution function. In case of BLG, $\rho(\varepsilon) = 2m/\pi\hbar^2$, $v_p = p/m$, which results in ordinary Drude conductivity

$$\sigma_{\text{BLG}} = \frac{ne^2\tau_p/m}{1 - i\omega\tau_p}. \quad (17)$$

In case of SLG, $\rho(\varepsilon) = 2\varepsilon/\pi\hbar^2 v_F^2$, $v_p = v_F$, and the conductivity reads

$$\sigma_{\text{SLG}} = \frac{e^2}{\pi\hbar^2} \frac{kT \ln(1 + e^{\varepsilon_F/kT})}{-i\omega + \tau_p^{-1}} \approx \frac{e^2}{\pi\hbar^2} \frac{\varepsilon_F}{-i\omega + \tau_p^{-1}}. \quad (18)$$

The latter equality is valid at low temperatures. Using the low-temperature relation between density and Fermi energy in SLG $n = \varepsilon_F^2/p\hbar^2 v_F^2$, we readily observe that classical conductivity of SLG is still given by the Drude formula (17) with density-dependent mass $m \rightarrow \varepsilon_F/v_F^2 \propto n^{1/2}$. Combining Eqs. (15), (17) and 18, we observe that plasma frequency in BLG scales as $\omega \propto n^{1/2}$, while in SLG $\omega \propto n^{1/4}$.

Supplementary Note 7: Resonance broadening and plasmon lifetime

Before discussing the physics beyond THz rectification, we specify mechanism-independent quantities, namely, the positions of plasma resonances and resonance width. Introducing the complex reflection phase

$$\exp[i\theta'_r - \theta''_r] = -r_s r_d, \quad (19)$$

we transform the "resonant denominator" in eq. (1) of the main text

$$R(\omega, V_g) \propto |1 - r_s r_d e^{2iqL}|^{-2} = \frac{1}{2} \frac{e^{\theta''_r + 2q''L}}{\cosh(\theta''_r + 2q''L) + \cos(\theta'_r + 2q'L)}, \quad (20)$$

The maxima of responsivity correspond to wave vectors

$$q'_0 = \frac{\pi}{2L}(2k + 1 + \theta'_r/\pi). \quad (21)$$

In the case of Dyakonov-Shur boundary conditions realized in our devices, $\theta_r = 0$, and the first resonance corresponds to L equal to the quarter of plasmon wavelength. Assuming reflection and scattering losses to be small, the lineshape (20) can be transformed to Lorentzian in the vicinity of each peak

$$R(\omega, V_g) \propto \frac{e^{\theta'_r + 2q''L}}{(q''L + \theta''_r/2)^2 + (q' - q_0)^2 L^2}. \quad (22)$$

The full width at half-height is given by

$$\frac{\delta q}{q_0} = \frac{1}{\omega\tau} + \frac{2 \ln |r_s r_d|^{-1}}{\pi(2k + 1)} \equiv \frac{1}{\omega\tau_p}, \quad (23)$$

here we have introduced the plasmon lifetime τ_p which is below the scattering time τ_p due to resonator loss. It is also possible to take into account the effect of finite antenna resistance on plasmon linewidth. To this end, one should transform resonant denominator of the form (14) in the vicinity of resonance. This leads us to

$$\frac{1}{\omega\tau_p} = \frac{1}{\omega\tau} + \frac{2 \ln |r_s r_d|^{-1} + 2Z'_a/Z'_{tl}}{\pi(2k + 1)}. \quad (24)$$

The above equation clearly demonstrates that inverse plasmon lifetime τ_p^{-1} is the sum of electron momentum relaxation rate τ^{-1} , contact damping rate

$$\tau_{\text{cont}}^{-1} = \frac{2\omega \ln |r_s r_d|^{-1}}{\pi(2k + 1)} = \frac{s}{L} \ln |r_s r_d|^{-1} \propto \sqrt{V_g}, \quad (25)$$

and damping rate due to antenna resistance

$$\tau_{\text{ant}}^{-1} = \frac{2s}{L} \frac{Z'_a}{Z'_{tl}} \propto V_g. \quad (26)$$

The two latter contributions to damping rate are minimized in the vicinity of charge neutrality point. Examples of calculated plasmon lifetime including the contributions of contacts and antenna are shown in Supplementary Fig. 6. Effects of radiative contribution to plasmon damping on detector responsivity is shown in Supplementary Note 9, along with the discussion of detection mechanisms.

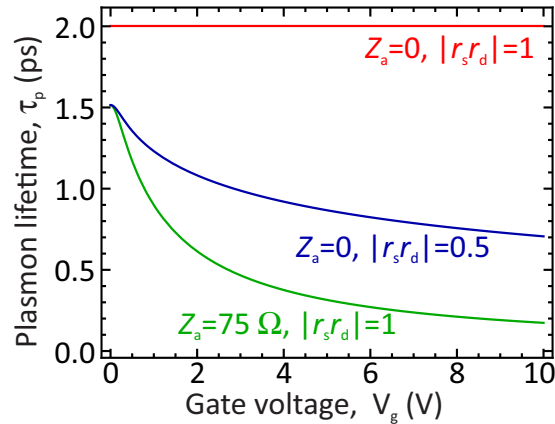


FIG. 6. **Plasmon damping.** Calculated plasmon lifetimes assuming momentum relaxation time $\tau = 2$ ps and no antenna and contact losses (red), lossless antenna and reflection coefficient $|r_s r_d| = 0.5$ (blue), antenna resistance $Z'_a = 75$ Ohm and perfect reflection (green). Plasmon velocity s at charge neutrality point is limited by residual carriers with density $n^* = 5 \times 10^{10} \text{ cm}^{-2}$.

As the wave vector at fixed frequency is inversely proportional to wave velocity, $q = \omega/s \propto V_g^{-1/2}$, expression (23) can be transformed to the voltage scale

$$\frac{\delta V_g^{-1/2}}{V_g^{-1/2}} = \frac{1}{\omega\tau_p}. \quad (27)$$

Supplementary Note 8: Photothermoelectric rectification in Fabri-Perot cavity

Asymmetric feeding of THz radiation results in asymmetric heating of the device and emergence of thermoelectric effect. The resulting dc voltage is³²

$$eV_{\text{pte}} = (S_{ch} - S_{cont}) [T_s - T_d], \quad (28)$$

where S_{ch} is the Seebeck coefficient in the gated channel, and S_{cont} – in the metal-doped graphene contact, T_s is the local temperature at the source junction and T_d is at the drain junction. From now on, we refer to the gated part of graphene as "channel" and ungated part – as "contact". The doping of ungated part does not depend on gate voltage, however, it can be non-uniform due to the effects of built-in field near metal contacts.

The temperature difference $T_s - T_d$ induced by non-uniform heating of the device can be found from the solution of heat transfer equation in the channel:

$$\frac{\partial^2 T}{\partial x^2} + \frac{T - T_0}{L_T^2} = -\frac{q(x)}{\chi_{ch}}, \quad (29)$$

$$(30)$$

where $q(x) = 2\text{Re}\sigma_\omega |E_{x\omega}|^2$ is the Joule heating power, χ_{ch} is the electron thermal conductivity in the channel, $L_T = (\chi_{ch}\tau_\varepsilon/C_e)^{1/2}$ is the thermal relaxation length, τ_ε is the energy relaxation time due to heat sink into substrate phonons⁵³, and C_e is the heat capacitance of the electronic system. Equation (29) is supplemented by the boundary conditions at the boundaries of gated domain

$$\frac{\chi_{cont}}{L_{cont}}(T_s - T_0) = \chi_{ch}\nabla T_s, \quad \frac{\chi_{cont}}{L_{cont}}(T_d - T_0) = -\chi_{ch}\nabla T_d; \quad (31)$$

these conditions follow from the continuity of heat flux at the interfaces. The sought-for temperature difference between source and drain can be obtained in the closed form under the following simplifying assumptions (1) the Joule heating occurs only in the channel (2) the temperature drop across the contacts is much less than maximum overheating in the channel. Both conditions are justified by the small length of the contacts $L_{cont} \ll L$. Under these assumptions, the expression for the photo-thermoelectric voltage acquires a physically appealing form

$$eV_{\text{pte}} = (S_{ch} - S_{cont}) \frac{l_{cont}}{\chi_{cont}} \int_0^L 2\text{Re}\sigma_\omega |E_{x\omega}|^2 \frac{\sinh \frac{x-L/2}{L_T}}{\sinh \frac{L}{2L_T}} dx. \quad (32)$$

The quantity χ_{cont}/l_{cont} is the thermal *conductance* of the contact, while the integral is the difference of heat fluxes traveling toward the source and toward the drain. The kernel of the integral is anti-symmetric with respect to the middle of the channel $x = L/2$, therefore, the PTE signal appears only due to asymmetric heating $q(x)$. Final evaluation of PTE voltage is performed by substituting the solution for electric field (12) into (32):

$$eV_{\text{pte}} = (S_{ch} - S_{cont}) \frac{2L_{cont}L_T\text{Re}\sigma_\omega}{\chi_{cont}} \frac{|q|^2 V_a^2}{e^{q''L + \theta_r''/2} |1 - r_s r_d e^{2iqL}|^2} \times \left[\sin 2\alpha' \frac{2q' L_T \cos q' L - \coth \frac{L}{2L_T} \sin q' L}{1 + (2q' L_T)^2} + \sinh 2\alpha'' \frac{2q'' L_T \cosh q'' L - \coth \frac{L}{2L_T} \sinh q'' L}{1 - (2q'' L_T)^2} \right], \quad (33)$$

where $\alpha = \theta_r + qL/2$.

Supplementary Note 9: Dyakonov-Shur rectification in Fabri-Perot cavity

The so-called Dyakonov-Shur rectification includes two physically different nonlinearities. One contribution to the rectified current appears due to simultaneous modulation of 2d channel conductivity and application of longitudinal field. This effect, also known as resistive self-mixing, results in the rectified voltage

$$V_{\text{rsm}} = 2\text{Re} \int_0^L \frac{1}{\sigma_{\omega=0}} \frac{d\sigma_\omega}{dV_{\text{gc}}} V_{-\omega}(x) \frac{\partial V_\omega(x)}{\partial x} dx. \quad (34)$$

Here $\sigma_{\omega=0} = ne^2\tau/m$ is the dc conductivity of a 2D channel, n is the carrier density, e and m are the elementary charge and effective mass of charge carriers respectively, τ is the momentum relaxation time, and $\sigma_\omega = \sigma_{\omega=0}/(1 - i\omega\tau)$ is the high-frequency conductivity. Evaluation of the integral leads us to the result

$$V_{\text{rsm}} = \frac{V_a^2/V_g}{\sqrt{1 + \omega^2\tau^2}} \frac{\frac{q''}{q'} [\cos \theta_r' - \cos(\theta_r' + 2q'L)] + \frac{q'}{q''} [\cosh \theta_r'' - \cosh(\theta_r'' + 2k''L)]}{2e^{\theta_r'' + 2q''L} |1 - r_s r_d e^{2iqL}|^2} \quad (35)$$

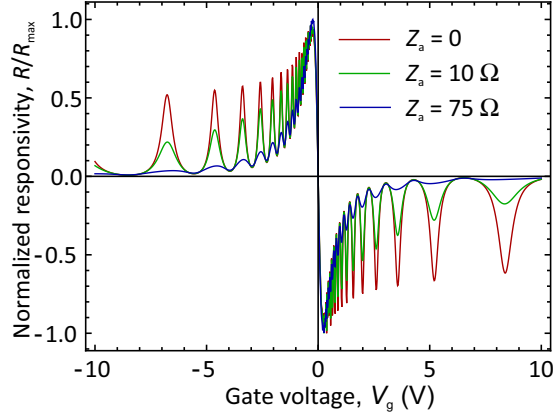


FIG. 7. **Dyakonov-Shur photoresponse.** Calculated Dyakonov-Shur responsivity of BLG FET detector as a function of gate voltage at different values of antenna impedance. All curves are normalized by their maximum value reached in the vicinity of NP. Parameters: channel length $L = 6 \mu\text{m}$, momentum relaxation time $\tau = 2 \text{ ps}$, radiation frequency $f = 2 \text{ THz}$, gate-channel separation $d = 80 \text{ nm}$, residual carrier density $n^* = 5 \times 10^{10} \text{ cm}^{-2}$.

Another contribution to rectified voltage stems from the difference of kinetic energies of electron fluid at the source and drain side (Bernoulli law). The underlying nonlinearity is manifested by convective term $(\mathbf{u}\nabla)\mathbf{u}$ in the Euler equation for electron fluid³. The corresponding rectified voltage is

$$eV_{\text{nl}} = \frac{e^2}{m^*(\omega^2 + \tau^{-2})} [|E_{x\omega}(L)|^2 - |E_{x\omega}(0)|^2], \quad (36)$$

where $E_{x\omega}$ is the complex amplitude of high-frequency longitudinal field in the channel given by (12). Using the result for electric field (12), we find

$$V_{\text{nl}} = \frac{1}{4} \frac{V_a^2/V_g}{\sqrt{1 + \omega^{-2}\tau^{-2}}} \frac{|1 + r_s r_d e^{2iqL}|^2 - |(1 + r_s r_d) e^{iqL}|^2}{|1 - r_s r_d e^{2iqL}|^2}. \quad (37)$$

Equations (35) and (37) generalize the known results of Dyakonov and Shur for arbitrary loading of the plasmonic FET at the terminals. Naturally, they reduce to the result of Ref. 3 for high-impedance drain load $\theta_r = 0$, yielding the photovoltage given by:

$$\Delta U = -\frac{1}{4} \frac{V_a^2}{V_g} \left[1 + \frac{2}{\sqrt{1 + (\omega\tau)^{-2}}} - \frac{1 + \frac{2 \cos 2q'L}{\sqrt{1 + (\omega\tau)^{-2}}}}{\sinh^2 q''L + \cos^2 q'L} \right], \quad (38)$$

The factor in square brackets peaks when the length of the FET channel matches odd multiples of the plasmon quarter-wavelength.

We note that Eqs. (35), (37) and (38) diverge as the dc gate voltage V_g tends to zero. In fact, this divergence stems from the gradual-channel approximation, relating carrier density and gate voltage $CV_g = en$, that fails near the charge neutrality point. The account of ambipolar transport involving electrons and holes leads to a simple replacement in Eqs. (35), (37) and (38):

$$\frac{1}{V_g} \rightarrow \frac{n/m_n^2 - p/m_p^2}{n/m_n + p/m_p} \frac{1}{s^2}, \quad (39)$$

where n and p are electron and hole densities, m_n and m_p are their effective masses, and $s^2 = (n/m_n + p/m_p)e^2/C$ is the plasma wave velocity in ambipolar system.

In the main text, the experimental photoresponse was compared with the DS photovoltage from eq. (38) corrected by eq. (39). The full picture of calculated Dyakonov-Shur photovoltage vs gate voltage is shown in Supplementary Fig. 7. Along with the result for perfect reflection from the drain and ideal voltage source ($Z_a = 0$, red line), it also shows the effect of finite antenna impedance on resonance width (green and blue lines). In accordance with the discussed antenna-induced "renormalization" of input voltage, eq. 13, the resonances at high carrier density are highly broadened due to finite Z_a . The width of resonances at low density, on the contrary, is mainly determined by momentum relaxation time.

Supplementary Note 10: Detector operation outside the linear regime

The data reported in the main text were obtained in the regime where the detector's photovoltage grew linearly with the power P of incoming radiation. With increasing P outside the linear regime, the heating of graphene's electronic system by high-frequency ac capacitive currents flowing between the source and gate terminals may affect the resulting responsivity. In order to reveal the role of heating, we have studied the response of our detectors at varying P and found that outside the linear regime, R_a decreases with increasing P . We attribute this decrease to the modification of the channel conductivity with increasing electronic temperature. To support this statement, we plot the FET-factor obtained by measuring the samples conductivity at different T inside the sample chamber. Clearly, R_a acquired at different P follows the evolution of the FET-factor F with T . This is reflected in the shift and decrease of the responsivity extrema with increasing P . We also refer to Fig. 2a of the main text which shows $R_a(V_g)$ at different T that resembles the behaviour shown in Supplementary Fig. 8.

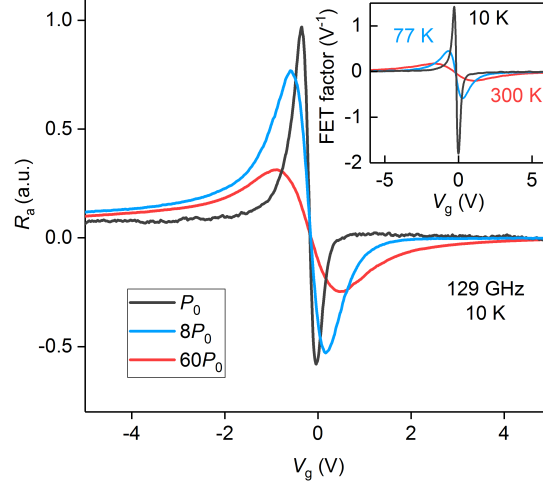


FIG. 8. **Role of electron heating.** Normalized to unity responsivity as a function gate voltage measured in one of our BLG detectors at given T and f for different P . $P_0 = 4 \mu\text{W}$. Inset: FET-factor as a function of V_g for different T .